Thesis for the Degree of Master of Science

The Molybdenum Nitride and Carbide Thin Films

by

Eunkang Jeong

Department of Chemistry

The Graduate School

Pukyong National University

Feburary 2016

The Molybdenum Nitride and Carbide Thin Films (몰리브데넘의 질화물 및 탄화물 박막)

Advisor: Prof. Yong-Cheol Kang

by

Eunkang Jeong

A thesis submitted in partial fulfillment of the requirements for the degree of

Master of Science

In Department of Chemistry, The graduate School,

Pukyong National University

February 2015

The Molybdenum

Nitride and Carbide Thin Films

A Dissertation

By

Eunkang Jeong

Approved by:

_____

(Chairman) Ju Chang Kim

_____ _____

(Member) Sang Yong Pyun (Member) Yong-Cheol Kang

February 26, 2016

Contents

LIST OF FIGURES

LIST OF TABLES

The Molybdenum Nitride and Carbide

Eunkang Jeong

Department of Chemistry, The Graduate School, Pukyong National University

Abstract

Molybdenum nitride (MoN_x) thin films were prepared on p-type Si(100) wafers using reactive radio frequency (rf) magnetron sputtering at various nitrogen gas ratios in an ultra high vacuum (UHV) system. Two metallic phases, Mo(110) and Mo(211), were detected from the film obtained without nitrogen gas in the sputter gas. The thickness of the films measured with a surface profiler decreased from 186.0 to 21.5 nm with increasing nitrogen gas ratio in the sputter gas from 0 to 100%, respectively. From the X-ray photoelectron spectroscopy (XPS) analysis, Mo species were further oxidized by the addition of nitrogen gas in the sputter gas. As nitrogen gas introduced, the portion of Mo^{4+} species decreased while those of Mo^{5+} and Mo^{6+} species increased. As the nitrogen gas ratio in the sputter gas increased, the formation of MoN_x thin films was confirmed by N 1s XPS spectra. The conductivity was decreased from 927.7 to 97.1 S/cm with 0 and 100% of nitrogen gas ratio, respectively.

Molybdenum carbide (MoC_x) thin films were deposited by rf magnetron co-sputtering in high vacuum chamber. Compare the properties of MoC_x thin films as the rf power changed on C target. The thickness of MoC_x thin films increased from 163.3 to 194.86 nm as C power was increased from 160 to 200 W. The crystallinity of

MoC_x were β-Mo_2C, Mo_2C, and diamond like carbon (DLC) structures observed by X-ray diffraction (XRD). The XPS data showed that the fabrication of MoC_x thin film was successful and the oxidation states of Mo and C were determined using high resolution XPS spectra of Mo 3d and C 1s. Mo 3d was consisted of metallic Mo, Mo^{4+}, and Mo^{6+}. And the deconvoluted C 1s peaks were assigned to C-Mo, C, C-O, and C=O phase.

Chapter I. Theories

1.1 X-ray photoelectron spectroscopy (XPS)

The XPS is one of the methods for study of surface characteristics such as low energy electron diffraction (LEED), scanning tunneling microscopy (STM), X-ray diffraction (XRD), and scanning electron microscope (SEM). The XPS is used for understanding the chemical environment like chemical composition, oxidation states, and chemical bonding of the elements on the surface [1.1]. Normally, the surface is adopted as the 10 monolayers within 10 nm in depth. The other part of the sample treated as the bulk material. The XPS is a surface sensitive technique. So, the XPS investigates surface characteristics such as the 10 nm depth in the material.

In Fig. 1.1, the schematic diagram depicts the principle of the generation of X-ray photoelectron from oxygen atomic layer. The oxygen has the three atomic orbitals labeled as 1s, 2s, and 2p. The X-ray source has the energy labeled as hυ.This energy is enough to eject the O 1s electron from the oxygen atom. The kinetic energy of the ejected electron can be determined by electron energy analyzer using the equation below,

$$E_k = h\nu - E_b - W_f .$$

The binding energy (E_b) of the electron in an atom is unique, so the XPS can analyze the chemical environment. And the symbol, W_f, denotes the work function of the sample. The work function is determined by the energy gap between E_v and E_f level.

The E_v denotes the vacuum level of the sample, and E_f denotes the Fermi level of the sample. After emission of the photoelectron from the sample, an Auger electron could be emitted. Fig. 1.2 describes Auger electron generation process. After a photoelectron is ejected by the X-ray, a hole is created in the 1s orbital. Then, the electron located at higher energy level than the 1s hole relaxes to fill the vacancy for stabilization. The energy difference between the vacancy level and ejected level can be used to eject another electron located at higher energy level. This ejected electron is called as an Auger electron. The kinetic energy of the Auger electron (E_A) can be determined by the following equation,

$$E_A = E_K - E_{L1} - E_{L2,3}.$$

The E_K is the binding energy of electron in the level K(1s), the E_{L1} and $E_{L2,3}$ are the binding energies of electron in level L_1(2s) and $L_{2,3}$(2p), respectively. The Auger electron on the Fig. 1.2 is called E_{KLL}. First electron ejected level is K. And the second relaxation electron level, L and the last ejected Auger electron level, respectively.

The X-ray photoelectron and Auger electron could be observed together in the wide range XPS spectra called as survey spectra. So, it is too difficult to distinguish X-ray photoelectron and Auger electron peaks. The X-ray photoelectron can be used to investigate the chemical composition of the sample. For the investigation process, differentiation of the X-ray photoelectron and Auger electron is required. The difficult of distinguishing can be solved by the equations used for XPS and Auger electron spectroscopy (AES). The equation used for XPS analysis is affected the energy of X-ray source ($h\upsilon$). But the equation for Auger electron

spectroscopy does not depend of the energy of X-ray source. So the problem of differentiation between X-ray photoelectron and Auger electron can be solved by switching X-ray source from Mg Kα to Al Kα, vice versa. In our laboratory, we used the dual anode X-ray source. The dual anode X-ray source consists of two types of anode, one is aluminum and the other is magnesium. Al and Mg sources have narrow band width of Kα line with 0.9 and 0.8 eV, respectively. They are good to apply for X-ray source. The one side of anode is coated with Al, the other side is coated with Mg, and the filament is placed around the anode. The electron ejected from the filament bombards the coated area, the X-ray (hυ) can be generated and impinges the sample surface. So, the X-ray photoelectron is ejected from the sample and the kinetic energy of the photoelectron can be investigated by an electron energy analyzer. A concentric hemispherical analyzer (CHA) is used in the XPS system. In our laboratory, the electron energy analyzer is normally used in constant analyzer energy (CAE) mode. The pass energy is controlled for survey and high resolution scan, 100~200 and 5~25 eV, respectively.

All the XPS processes are operated in the vacuum system. It's very important and necessary. The high vacuum system makes a long mean free path of electron. This vacuum environment is achieved by rotary vane pumps (RP), turbo molecular pump (TMP), two ion pumps (IP), and Ti sublimation pumps (TSP).

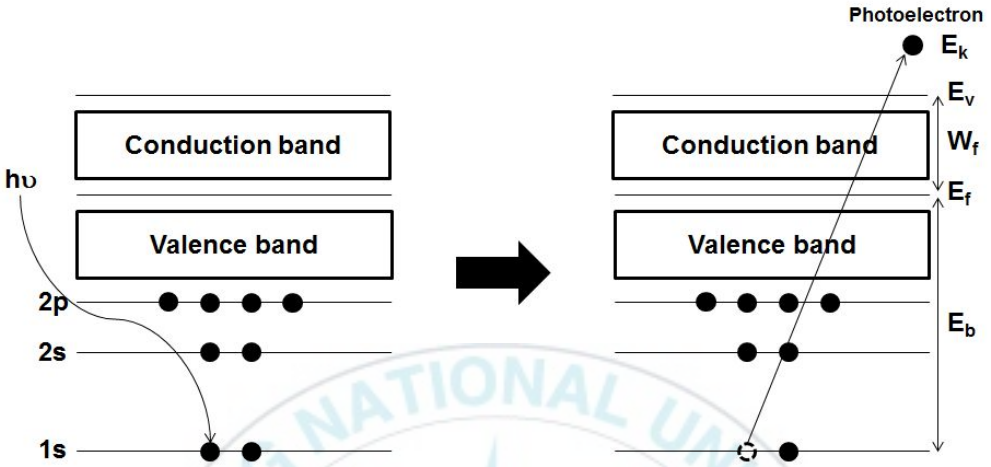

Fig. 1.1 Conceptual diagram of the generation of X-ray photoelectron from oxygen atom.

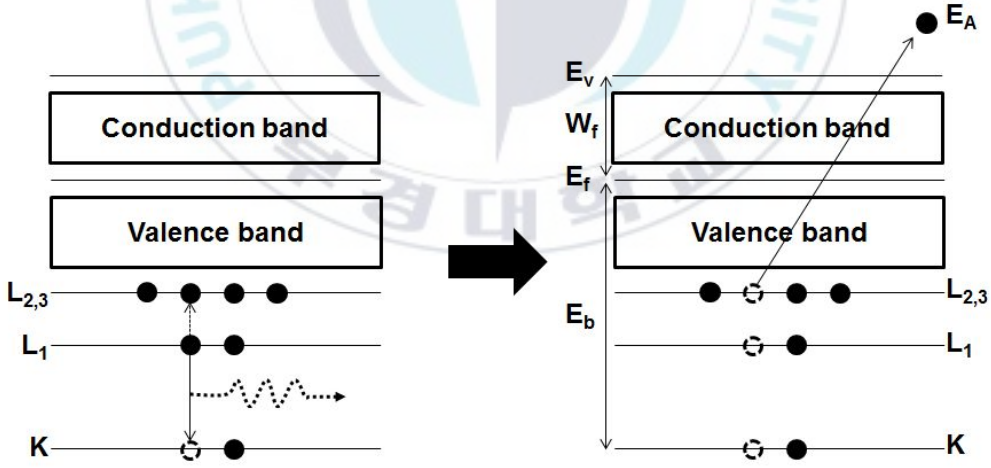

Fig. 1.2 The Auger electron ejected process after X-ray photoelectron ejected from the O 1s.

1.2 Radio frequency magnetron reactive sputtering

Thin films industry was increased by their easy application to many fields. Thin films can be applied for solar cells [1.2], semiconductors [1.3], field effect transistor [1.4], light emitting diode [1.5], and others. Thin films can be prepared by many methods such as sol-gel method like spin coating [1.6], roll-to-roll [1.7], chemical vapor deposition [1.8], and physical vapor deposition method [1.9]. Radio frequency (rf) magnetron reactive sputtering method is one of the physical vapor deposition methods.

The principle of rf magnetron reactive sputtering can be explained by this name. When energetic charged particles bombard target material, the component of target material can be sputtered out as neutral or charged particle to deposit. This process is called as sputtering. In general, the energetic charged particle is made from Ar gas. When the energetic particle is energized and ionized by rf, this process is called as rf sputtering. The sputtered target material will be deposit onto substrate such as silicon wafer or soda-lime glass. In order to use vacuum chamber for sputtering process, high vacuum (HV) system is required. The high vacuum is achieved by a rotary vane pump (RP) and a turbo molecular pump (TMP).

The sputtering method can take two types of power suppliers. One is the direct current (dc), and the other is rf. The power is applied on the target to be depositted on the substrate. The dc power can be applied only for conductor targets such as metal targets. The rf power, however, can be applied for not only conductors but insulators. And the rf power enhances the sputtering yield. The rf power used in this research was 13.56 MHz.

The magnetron is used for enhancing the sputtering yield as same reason of rf power. The magnetron is located on the back of the cathode (target material). Due to the magnetic field from the magnetron, the sputtering gas is bombarded targets repeatedly. So the sputtering efficiency increased. The reactive gas is injected to the sputtering chamber as a mixture with sputtering gas during sputtering process. In order to make metal oxide thin films, oxygen gas is introduced into the sputtering chamber with Ar gas during sputtering process. The sputtered target material reacts with the oxygen gas and deposited on the substrate as metal oxide phase. The mixture gas is controlled by a mass flow controller (MFC).

The schematic diagram of the rf magnetron reactive sputtering chamber used in this work is shown in Fig. 1.3. A is the main chamber of the rf magnetron reactive sputtering. In this chamber, three sputtering targets were installed for co-sputtering process. The pressure of the sputtering chamber was kept with using a TMP (B) and a RP (C). Pressure of the chamber was measured by D and E. The convectron gauge (D) can measures the pressure in the chamber in the range from atmospheric pressure to 10^{-3} Torr. The ionization gauge, marked E, measured the pressure in the range from 10^{-6} to 10^{-12} Torr. Fs are the rf power suppliers and can control the sputtering power applied on the targets individually. Shown as G, the rotator motor is used for rotation of substrate for uniform deposition. The H is the cooling system of the sputtering process.

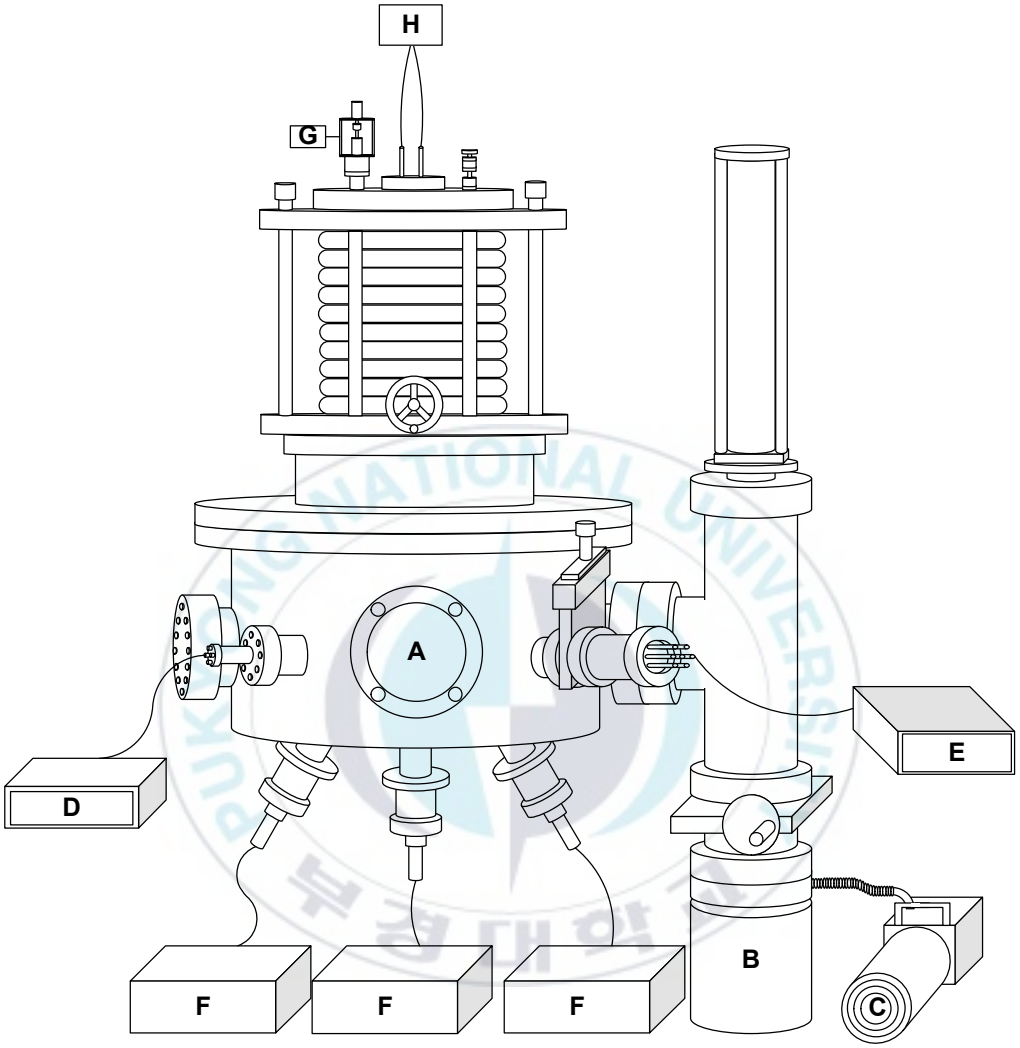

Fig. 1.3 The schematic diagram of the rf magnetron reactive sputtering chamber.

Chapter II. Deposition of molybdenum nitride thin films (MoN_x) using rf magnetron reactive sputtering method

2.1 Introduction

The molybdenum nitride (MoN_x) thin film has the good properties such as γ –Mo_2N phase has good cell potential [2.1], low resistivity [2.2], and hardness [2.3]. For these properties, the MoN_x thin films are applied at various fields such as an anode of Ni batteries [2.4], catalysts [2.5,2.6], and diffusion barriers [2.7-2.14]. The MoN_x is synthesized by various methods such as hydrothermal method [2.5], cathodic arc evaporation (CAE) method [2.12], chemical solution method [2.13], high temperature plasma method [2.15], and sputtering method [2.2,2.3,2.7-2.11,2.16-2.20]. The most of former studies were taken the sputtering method because it can be performed in low-temperature and large-area substrate. These advantages make sputtering method possible to apply in many laboratories and industries.

Previous reported experiment about preparation of MoN_x thin films adapted sputtering methods. Anitha *et al.* fabricated MoN_x thin films by rf magnetron sputtering at various nitrogen gas flow ratio. The phase of MoN_x thin films was determined by XRD as Mo_2N with several phases. The resistivity of thin films was increased from 0.26 to 6.00 μΩm as increasing nitrogen gas ratio from 0 to 89% [2.3]. Kumar *et al.* prepared the MoN_x thin films with nitrogen gas flow rate increased from 0 to 20 sccm by reactive dc magnetron sputtering method. The thickness of MoN_x thin films were decreased as nitrogen gas ratio increased. The crystallinity was changed as

nitrogen gas ratio changed from γ-Mo_2N(111) to β-Mo_2N(200), Mo_3N_2(111), $Mo_{16}N_7$(400), β-Mo_2N(220), and Mo_5N_6(110), to $Mo_{16}N_7$(400). Resistivity, one of the electrical properties, was increased from 3.0×10^{-9} to 1.8×10^{-6} Ωm as nitrogen ratio increased from 0 to 33%, respectively [2.8]. However, they did not give any information about composition and oxidation states of Mo prepared on the surface.

In this section, we report about fabrication the MoN_x thin films at various nitrogen gas ratios in ultra high vacuum (UHV) chamber is reported. The prepared MoN_x thin films were investigated by XPS for chemical composition and oxidation state of MoN_x thin films surface with different nitrogen gas ratio, crystallization of the MoN_x thin films were studied with XRD, the surface profiler used for measuring the thickness of deposited thin films, and the electrical properties were measured with a 4-point probe system.

2.2 Experimental details

The p-type Si(100) substrate was used for the substrate of MoN_x thin films after cleaned with acetone and dried with nitrogen gas. The sputtering gas was consisted of nitrogen (99.99%) and argon (99.99%) with various gas ratios as the total gas flow rate was fixed at 7 sccm. The MoN_x thin films were prepared by reactive radio frequency (rf, 13.56 MHz) magnetron sputtering at various nitrogen flow rates from 0 to 7 sccm controlled by a MFC. From hereafter, the MoN_x thin film deposited with X% of nitrogen gas flow rate of sputtering gas mixture ($N_2/(N_2+Ar)\times100$) will be called as MoN-X. In order to remove the contaminants in the sputtering chamber, rf sputtering was conducted in ultra high vacuum (UHV) chamber. The base pressure

of the chamber was kept less than 1.5×10^{-8} Torr. The base pressure was maintained by a RP, a TMP, and an IP. During the sputtering process, total working pressure (N_2+Ar) was kept at 45 mTorr. Sputtering target was the pure molybdenum target (99.95%, Tasco) with 50 mm diameter, 5 mm thickness, and supplied 100 W rf power. Before the sputtering process, pre-sputtering was performed for 10 min for stabilizing the plasma and cleaning the target as the shutter was closed. Then rf sputtering was conducted for 10 min to deposit MoN_x thin film on the Si substrate.

The XPS (ESCALab MKⅡ, VG, UK) was used for investigation of the chemical composition of MoN_x. The XPS used Mg Kα X-ray source (1253.6 eV). The base pressure of XPS system was kept under 3×10^{-10} Torr by a RP, a TMP, two IPs, and a TSP. The wide range XPS spectra called as survey spectra were taken for the qualitative analysis of samples. The survey spectra was collected with 100 eV pass energy, 100 ms dwell time, 0.5 eV energy step, and 4 times scan for increasing the signal to noise ratio. The narrow range spectra called as high resolution spectra was taken for specific atomic spectra. The range of the high resolution spectra was determined following the survey scan spectra information. High resolution XPS spectra were taken with a pass energy of 50 eV, energy step of 0.05 eV, scanned 9 times, and the other parameters were kept the same as the survey scan. For details of atomic ratio of N and O, and the oxidation states of Mo, deconvolution method was conducted with XPSPEAK41 software (ver 4.1) applied with 30% Gaussian/Lorentzian ratio. The surface profiler (alpha step-500, Tencor, USA) was applied for measured thickness of MoN_x thin films. The crystallinity of the thin films was investigated by XRD (X'Pert MPD system, PHILPS, Netherlands). Cu Kα

radiation and a step of 0.1 degree were used for XRD study. Electrical properties were measured by a 4-point probe measurement (MCP-T6000, Loresta, Netherlands).

2.3 Results and Discussion

The thickness of the obtained MoN_x thin films were measured by a surface profiler and determined after Grubbs test at 95% of confidence level as shown in Fig. 2.1 [2.20]. The thickness of MoN_x thin films were decreased as the nitrogen gas flow rate (N_2/N_2+Ar) increased. The nitrogen gas flow rate increased, then Ar gas portion in sputtering gas mixture was decreased. This decreased the sputtering yield of Mo target. And the decrease of sputtering yield caused decreasing ionized atom of the target material. So, the thickness of the MoN_x thin films was decreased as Ar gas portion decreased.

The crystallinity of MoN_x thin films was investigated with XRD as shown in Fig. 2.2. In all X-ray diffraction spectra, Si(311) [JCPDS #80-0018] peaks of substrate were evolved at around 56.6°. At spectra of MoN-0 thin film preparation without the reactive gas, shown two types of metallic Mo crystalline phases. The two metallic Mo phases are assigned for Mo(110) and Mo(211) [JCPDS #42-1120] phases centered at the diffraction angles of 40.8°and 74.0°, respectively. After MoN-21, nitrogen gas was introduced in the sputtering gas, two metallic Mo peaks were disappeared and three peaks were evolved at around 37.5°, 43.5°, and 63.1°. These three peaks are assigned for γ-Mo_2N(111), γ-Mo_2N(200), and γ-Mo_2N(220) evolved at around 40.0°, 44.0°, and 63.4°, respectively [JCPDS #25-1366].

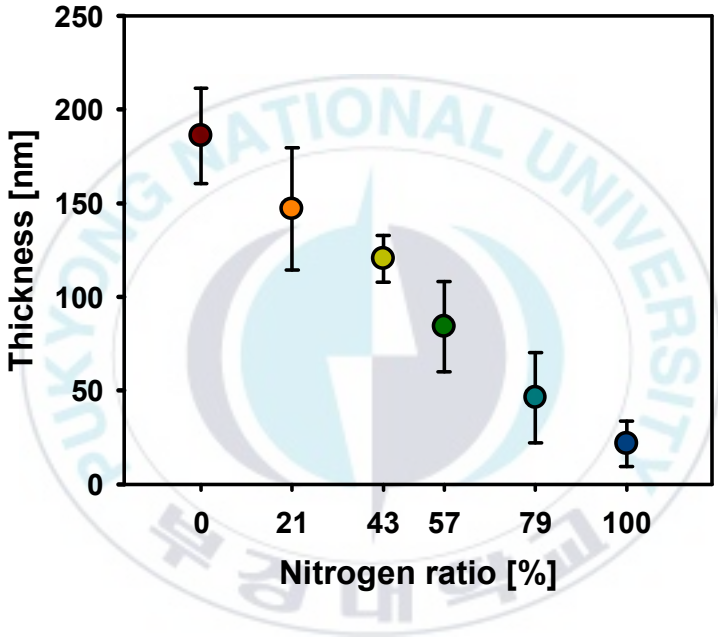

Fig. 2.1 Thickness of the MoN_x thin films as a function of nitrogen gas ratio in the sputtering gas.

All γ-Mo_2N peaks slightly shifted to lower diffraction angle and the intensities of the peaks were decreased as nitrogen gas flow rate increased because the crystallite sizes of structure were decreased. The crystallite sizes were calculated by using Debye-Scherrer's equation and the results are listed in Table 2.1[2.22]. The Debye-Scherrer's equation is given as:

$$D = 0.9\lambda / \beta \cos\theta \ .$$

The crystallite size (D, nm) is calculated with wavelength (λ, nm) of X-ray source (Cu Kα, 0.154 nm), full width at half maximum (FWHM, β, rad) of peak, and diffraction angle (θ).

The reason for this phenomenon could be explained by the Hagg's structure. The Hagg's structure was consisted the structure of transition metal elements and some material such as nitrogen, carbon fill the interstitial sites [2.10,2.23]. As the nitrogen contents in the sputter gas increased, the probability to occupy the octahedral interstitial sites of γ-Mo_2N increased. Therefore, the crystal structure of γ-Mo_2N was defective with the interstitial nitrogen and the crystallite size decreased. During rf sputtering at high ratio of nitrogen in the sputtering gas, excess octahedral sites could be occupied by nitrogen atoms, resulting the formation of defective γ-Mo_2N [2.10].

The XPS survey spectra of MoN_x thin films with nitrogen gas flow rate changed and UHV system for a clean environment was shown in Fig. 2.3. The XPS peaks of C 1s and O 1s (centered at 284.5 and 531.0 eV) were rarely detected. Therefore, the sputtering process for preparing the MoN_x thin films were conducted in a nearly contamination free environment by applying UHV system. The investigated

XPS peak of Mo 3d and Mo 3p at 230.5 and 397.6 eV were observed. The Mo $3p_{3/2}$ peaks were difficult to identify N 1s in the survey XPS spectra, because the binding energy of N 1s electron was nearly of Mo $3p_{3/2}$ electron centered. However, the peak intensity of Mo $3p_{3/2}$ and N 1s more increased as Mo $3p_{1/2}$ peak intensity increased with nitrogen ratio increased. This phenomenon appeared that Mo nitride was successfully prepared on the Si(100) substrate. For clarifying about nitrogen exists in the thin films, high resolution XPS spectra at the binding energy area of Mo 3p and/or N 1s were taken and deconvoluted based on the results of the high resolution spectra of Mo 3d spectra shown in Fig. 2.5 [2.24]. The atomic ratio of Mo species with various oxidation states was inferred from high resolution XPS spectra of Mo 3d shown in Fig. 2.4.

High resolution XPS spectra of Mo 3d were shown in Fig. 2.4(a). The Mo $3d_{5/2}$ peak shifted to higher biding energy after nitrogen gas was introduced in sputtering gas. To get the reason of shifted the peak and detail chemical oxidation information, peak deconvolution process was performed. The representative deconvoluted spectra of Mo 3d for finding oxidation states are shown in Figs. 2.4(b) and detail deconvoluted information are shown in Table. 2.2. Two types of Mo oxidation states were existed in MoN-0 and those are assigned for Mo^{4+} and Mo^{5+}, they were centered at 230.0 eV and 231.3 eV, respectively. The two phase of oxidation Mo was formed as MoO_2 and Mo_2O_5, respectively [2.25,2.26]. After nitrogen gas was introduced, from MoN-21, the atomic ratio of Mo^{4+} decreased while Mo^{5+} increased and Mo^{6+} evolved centered at 232.7 eV [2.27,2.28]. The oxygen in MoO_2 was replaced with nitrogen in sputtering gas to form Mo_3N_4 without changing

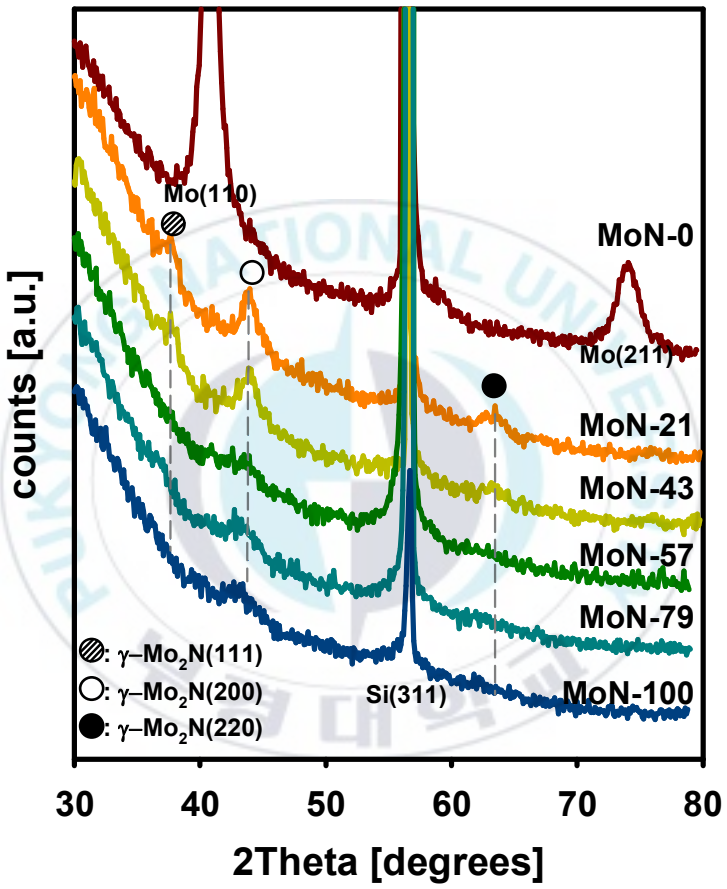

Fig. 2.2 The crystallinity of MoN_x thin films

Table. 2.1 The information of XRD spectra about MoN_x thin films.

Sample	Phase	Diffraction Angle [2θ deg]	Crystallite Size [nm]
MoN-0	Mo(110)	40.8	6.5
	Mo(211)	74.0	4.5
MoN-21	γ-Mo_2N(111)	37.9	4.0
	γ-Mo_2N(200)	44.0	4.8
	γ-Mo_2N(220)	63.4	3.5
MoN-43	γ-Mo_2N(111)	37.8	3.8
	γ-Mo_2N(200)	44.0	5.4
	γ-Mo_2N(220)	63.3	3.1
MoN-57	γ-Mo_2N(111)	43.9	3.9
	γ-Mo_2N(200)	62.9	2.7
MoN-79	γ-Mo_2N(220)	43.9	2.9
MoN-100	γ-Mo_2N(220)	43.5	2.8

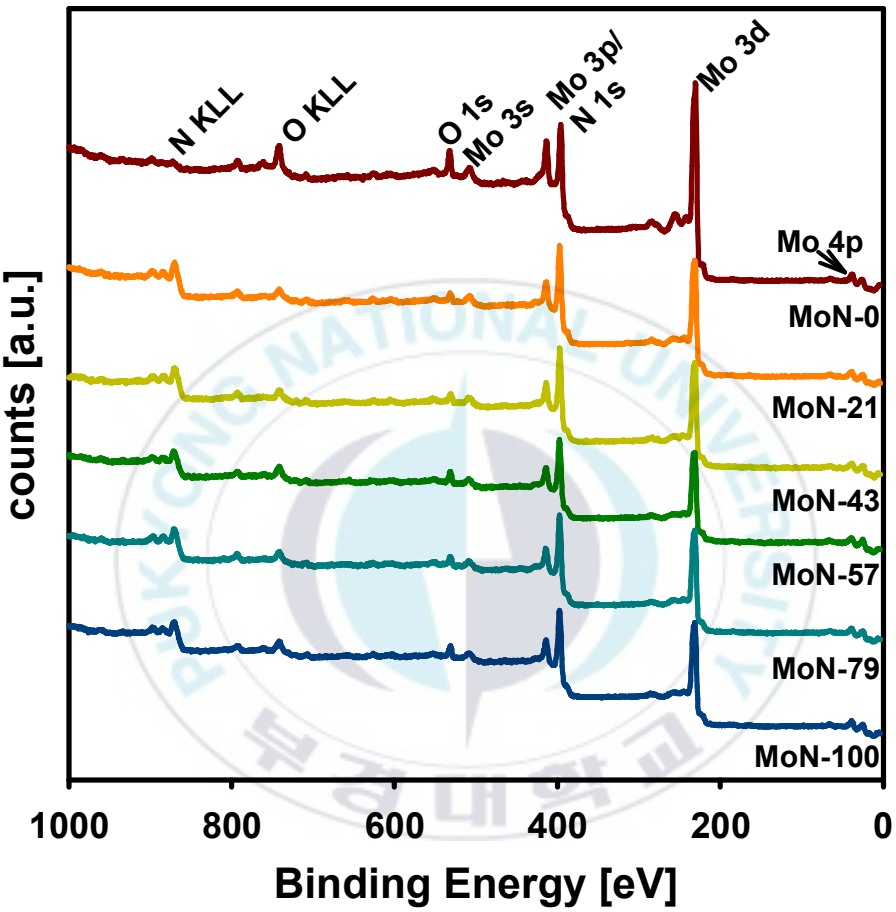

Fig. 2.3 The XPS survey spectra of the MoN_x thin films prepared with changing the nitrogen gas flow rate.

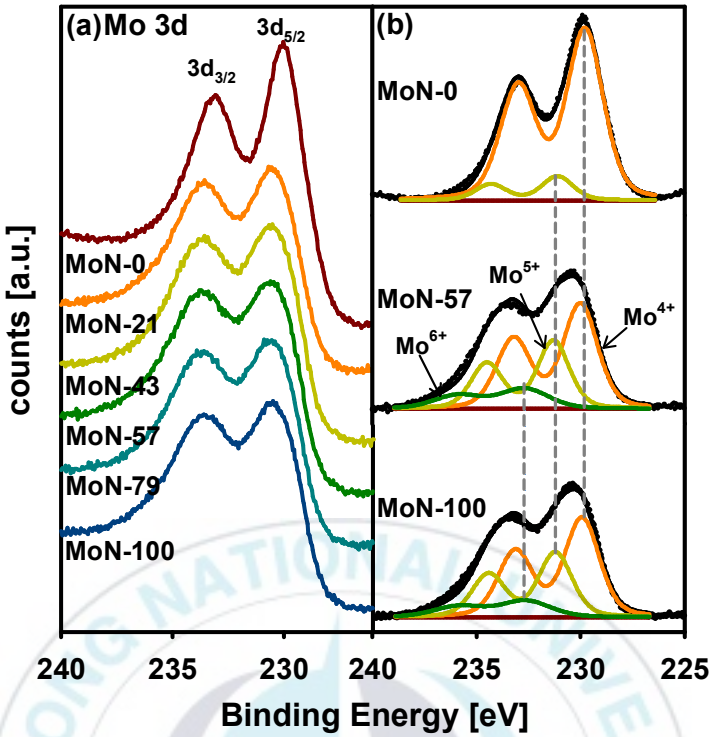

Fig. 2.4 (a) is the narrow spectra of the MoN_x thin films and (b) was shown the representative deconvolution data of Mo 3d in MoN_x thin films.

Table. 2.2 Detailed information about the deconvolution data of Mo 3d

		B.E. [eV]	FWHM [eV]	Sample					
				MoN -0	MoN -21	MoN -43	MoN -57	MoN -79	MoN -100
Mo $3d_{5/2}$	Mo^{4+}	230.0 (±0.2)	2.0 (±0.1)	89.2	58.0	59.9	53.6	54.9	53.5
	Mo^{5+}	231.3 (±0.2)	1.8 (±0.1)	10.8	29.9	29.9	32.0	32.8	33.7
	Mo^{6+}	232.7 (±0.1)	2.8 (±0.1)	-	12.1	10.2	14.4	12.3	12.8

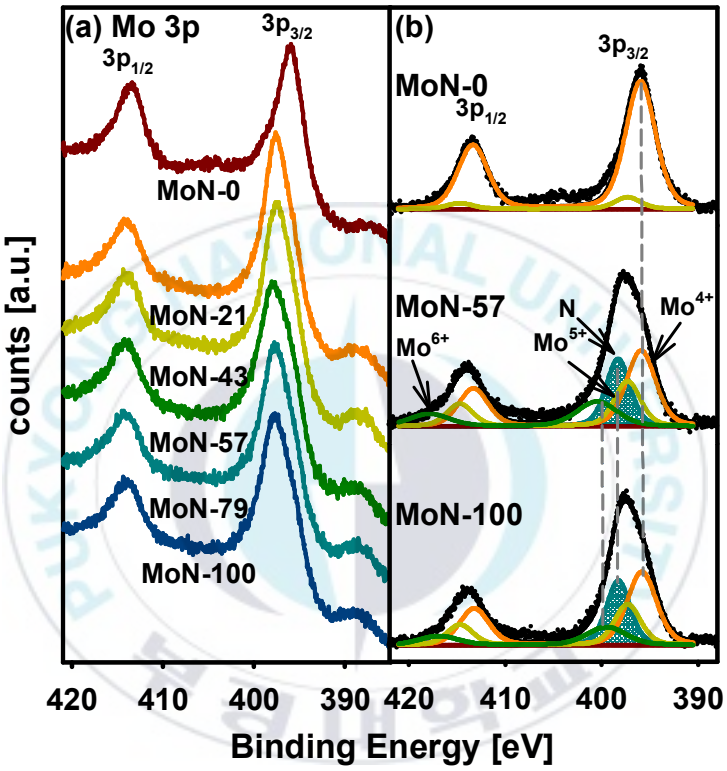

Fig.2.5 (a) is the Mo 3p and/or N 1s narrow spectra of MoN_x thin films and (b) is the representative deconvolution data of MoN_x as nitrogen gas flow changed

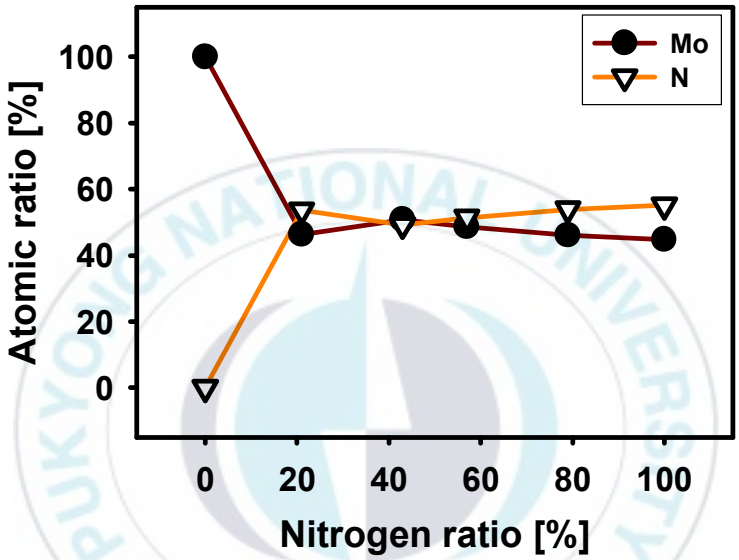

Fig. 2.6 Atomic percentages between Mo and N in the MoN_x thin films.

the oxidation state of Mo. Also, the Mo_2O_5 was changed to MoON and Mo^{6+} was evolved as the form of MoN_2 by introduction of nitrogen gas. The reactive nitrogen gas affects to oxidize Mo species. This caused that the oxidation state of Mo species changed from low oxidation state (Mo^{4+}) decreased to increase Mo^{5+} and Mo^{6+} as shown in Table. 2.2 and Fig. 2.7.

The Mo $3p_{3/2}$ shifted to a higher binding energy as nitrogen gas introduced during sputtering process like the shift of Mo $3d_{5/2}$ as shown in Fig. 2.5(a). For calculating the oxidation state of Mo and nitrogen, deconvolution process was conducted refer with Mo 3d oxidation state ratio and representative deconvolution data are shown in Fig. 2.5(b). After calculating the total area of Mo species with different oxidation states from the Mo 3p peak area and/or N 1s, the portion of nitrogen was obtained and shown in Fig. 2.6. In this figure, the nitrogen concentration in the MoN_x thin films was increased after MoN-21. The N/Mo ratio was reached nearly to 1 as nitrogen gas introduced in the sputter gas. The stoichiometric ratio of N to Mo for γ- Mo_2N is 0.5. The structure of γ-Mo_2N consisted of fcc structure with Mo and half-fully octahedral interstitial sites with Nitrogen. Then, the extraneous nitrogen atoms in our MoN_x thin films occupy the unfilled octahedral interstitial sites of the γ-Mo_2N structures. This XPS results are well correlated with the XRD results discussed earlier. Electrical properties of MoN_x thin films were measured with a four point probe system and shown in Fig. 2.8. The conductivity and resistivity shown the opposite tendency. The tendency of conductivity is similar to that of atomic ratio of Mo^{4+} species shown in Fig. 2.7. After nitrogen gas involved in the sputter gas, conductivity was monotonically increased as a function of nitrogen gas flow rate.

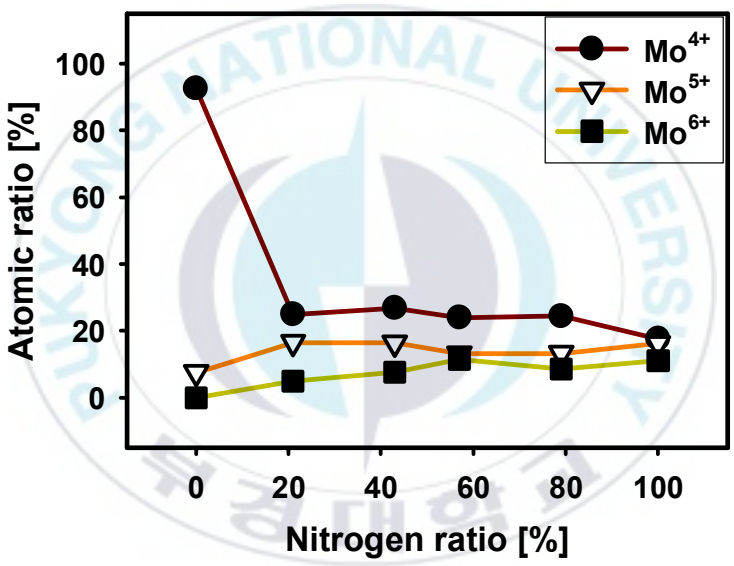

Fig. 2.7 Atomic percentages of the Mo with different oxidation states in the MoNx thin films.

2.4 Conclusion

The phases of MoN-0 were metallic Mo(110) and Mo(211). When nitrogen gas was introduced, the metallic phases diminished and γ-Mo_2N phases emerged. The crystallite size decreased as the nitrogen gas ratio increased. This phenomenon could be explained by Hagg's structure. The thickness of the films decreased from 186.0 nm for MoN-0 to 21.5 nm for MoN-100 by using the alpha step measurement. From the XPS analysis, Mo species was oxidized as nitrogen gas was introduced. Mo^{4+} and small portions of Mo^{5+} species were prevalent in MoN-0. Further oxidized species, Mo^{6+}, was detected and the amount of Mo^{6+} increased while that of Mo^{4+} decreased as the nitrogen gas ratio was increased. Atomic ratio of N to Mo was nearly 1. These results are well correlated with XRD results. Conductivity and resistivity of MoN_x films showed opposite propensity. The varying propensity of conductivity is similar to that of atomic ratio of Mo^{4+} species. Conductivity was decreased from 927.7 S/cm for MoN-0 to 27.3 S/cm for MoN-1.5. Then conductivity of MoN_x thin film was monotonically increased as nitrogen gas flow rate increased.

Chapter III. Deposition of molybdenum carbide thin films (MoC_x) using rf magnetron co-sputtering method

3.1 Introduction

Molybdenum carbide (MoC_x) has been applied in many fields such as diffusion barrier [3.1-3.3], atomic mirror [3.4,3.5], hard coating [3.1,3.6,3.7], and catalyst [3.8] because of its hardness, resistivity, and Mo_2C phase doing like Pt catalyst property [3.1,3.8,3.9]. Noble-metal like morphology of MoC_x was reason of application for catalyst [3.8]. The most previous works used chemical vapor deposition (CVD) and physical vapor deposition (PVD) method with assistance of CH_4 as a reactive gas for the preparation of MoC_x thin films [3.1,3.2,3.6,3.7,3.10-3.20].

Ji *et al.* prepared MoC_x thin films using the unbalanced magnetron sputtering with inductively coupled rf plasma CVD assisted with CH_4/Ar at various sputtering current on Mo target [3.21]. The crystallization of MoC_x thin film were consist of MoC(100) and diamond-like carbon (DLC) structure. The molybdenum and molybdenum carbide atomic ratio were increased as sputtering current increased, investigated by XPS. And D peak and G peaks were investigated by Raman spectroscopy. In Raman experiment, D peak was shift to G peak as sputtering current was increased. So, the intensity ratio of D/G was decreased. Intensity ratio of D/G was mean of sp^3 bond phase. The sp^3 bond of C was decreased on MoC_x thin films. Roughness of the MoC_x was increased as sputtering current increased investigated by

atomic force microscopy (AFM).

Alberto *et al.* made Mo_2C catalyst according to the following procedure. An appropriate amount of ethanol was added $MoCl_5$, for forming the metal orthoesters [3.8]. Metal orthoesters was mixed with solid urea and urea gels, and heated at 800 ^oC with nitrogen gas flow for 3 hr. Mo_2C phase was investigated by XRD. And Mo_2C phase was compare the ability as catalyst with Pt and Ru. Mo_2C was active as catalyst for benzyl alcohol conversion until 6 hour, and 80% conversion of benzylalcohol. They investigated crystallization of Mo_2C after active as catalyst. Mo_2C phase was decreased as MoO_3 increased after activity as catalyst. MoO_3 was active like Mo_2C but showed lower activity than Mo_2C phase. Pt and Ru have selectivity for oxidation of benzyl alcohol to benzaldehyde. On the contrary, Mo_2C phase has selectivity for dehydration benzyl alcohol to benzyl ether. Mo_2C phase has another selectivity effected by temperature. Temperature at 60 ^oC, benzaldehyde selectivity was increased nearly 39%. The temperature at 100 ^oC, benzaldehyde selectivity was decreased to 19%, on the contrary benzyl ether selectivity increased to 70%.

This paper reports about the fabrication of MoC_x thin films on Si(100) substrate by means of rf magnetron co-sputtering using C and Mo targets. The MoC_x thin films were obtained at various rf powers on C target without using CH_4 reactive gas in high vacuum chamber (HV). We investigated the chemical composition and crystallinity of MoC_x thin films using XPS and XRD, respectively. The thickness, electrical properties, and the surface free energy (SFE) of the thin films were investigated by using alpha step measurement, four point probe measurement , and contact angle measurement using distilled water (DW) and ethylene glycol (EG), respectively.

3.2 Experimental details

The MoC_x thin films were deposited on p-type Si(100) as a substrate which is cleaned by chemical method and dry with nitrogen gas prior to install in co-sputtering chamber. The MoC_x was deposited by rf (13.56 MHz) magnetron co-sputtering method. During the sputtering process, substrate temperature was maintained at 60 ^oC by a temperature controller. And the substrate was rotated at 12 rpm for uniform deposition. For co-sputtering method, two types of targets were used; Carbon (99.5%, Tasco) and Molybdenum (99.95%, Tasco). Both sputtering targets have a diameter of 50 mm and a thickness of 5 mm. The rf power on Mo target was optimized at 30 W for whole co-sputtering process. Then, the power on C target was varied 160 to 200 W with a 10 W of increment. From hereafter, the MoC_x thin films obtained at X W of rf power on C target will be referred as MoC-X.

Ar gas was used for sputtering gas without reactive gas such as CH_4. The flow rate of Ar was controlled by a MFC and fixed at 20 sccm. Base pressure of the co-sputtering chamber was kept less than 7×10^{-7} Torr, and working pressure was maintained between 24.9 and 25.2 mTorr by a RP and a TMP. For cleaning the co-sputtering chamber, the chamber was heated by heating wire with 150 V power for 30 min to evacuate the contaminants before every experiment. Pre-sputtering was performed for 10 min to clean the targets and to stabilize plasma as the shutters were closed. After pre-sputtering, co-sputtering for deposition of MoC_x was carried out for 1 hr as the shutters open.

The thickness of MoC_x thin films were measured with a surface profiler (alpha step-500, Tencor, USA). The crystallinity of MoC_x thin films was investigated

by XRD (X'pert –MPD system, Philips, Netherlands) with glancing mode. Cu Kα radiation and 0.05 degree of step size were applied for XRD study. The chemical environment of MoC_x thin films was investigated by XPS (ESCALab MKII, VG, UK). Mg Kα X-ray source (1253.6 eV) was used for the XPS. The base pressure of the XPS system was kept around 3×10^{-10} Torr by a RP, a TMP, two IP, and a TSP. For qualitative investigation of thin films, wide spectra scan called as survey scan was conducted. The survey XPS spectra were collected with a pass energy of 100 eV, dwell time of 100 ms, and an energy step of 0.5 eV. The XPS survey spectra were obtained after scanning 4 times to increase the signal to noise ratio. The detailed information of each atoms, narrow spectra scan called as high resolution scan was performed. High resolution XPS spectra were taken with a pass energy of 50 eV, an energy step of 0.05 eV, scanned 9 times, and the other of parameters were kept the same as survey scan. For detailed chemical information of MoC_x thin films, the high resolution XPS spectra of C and Mo were deconvoluted by using XPSPEAK41 software (ver 4.1) in 30% of Gaussian/Lorentzian ratio. The electrical properties were measured with a 4-point probe system (MCP-T600, Loresta, Netherlands). And contact angles of DW and ethylene glycol EG were measured to determine the surface free energy of MoC_x films using home-made contact measurement system.

3.3 Results and Discussion

Fig. 3.1 shows the thickness of MoC_x thin films deposited on p-type Si(100) substrate at various rf powers on C target (160 to 200 W) and fixed rf power on Mo target (30 W) for 1 hr. The thickness of the MoC_x thin films was measured by alpha step measurement and determined after Grubbs test at 95% of confidence level [3.22].

As shown in Fig. 3.1, the thickness of MoC_x thin films was increased from 163.27 to 194.68 nm when the rf power on C target increased, respectively. This phenomenon can be explained that the power on C affected to the velocity of Ar ion in plasma and sputtering rate of carbon was increased. This caused the thickness of the MoC_x thin films was increased as the rf power of carbon target increased.

The crystallinity of MoC_x thin films was investigated with XRD as shown in Fig. 3.2. The crystalline phase of carbon was observed as DLC phase. The DLC phase is assigned for DLC(107) [JCPDS #79-1473]. The intensity of the phase was increased as rf power increased. Two MoC_x crystalline phases were assigned for β-Mo_2C(121) [JCPDS #45-1013] and Mo_2C(200) [JCPDS #79-0744] at the diffraction angles of 28.12° and 36.63°, respectively. The MoC_x phases were consisted of body centered cubic (bcc) structure with Mo. The Mo structure has the interstitial site such as octahedral and was filled with carbon. If the any atom can be filled the interstitial site, the atomic radii between Mo and atom will be under 0.59. The atomic radii ratio between Mo and carbon is 0.556 [3.23]. So, the MoC_x phases can be explained the interstitial carbide structures. The intensity of β-Mo_2C(121) phase was slightly decreased as rf power increased. Mo_2C(200) phase at 36.63° were slightly shifted to law diffraction angle as rf power increased. Then, crystallite sizes did not change significantly. The detailed information about Mo_2C(200) crystallite size, FWHM, diffraction angles were listed in Table 3.1.

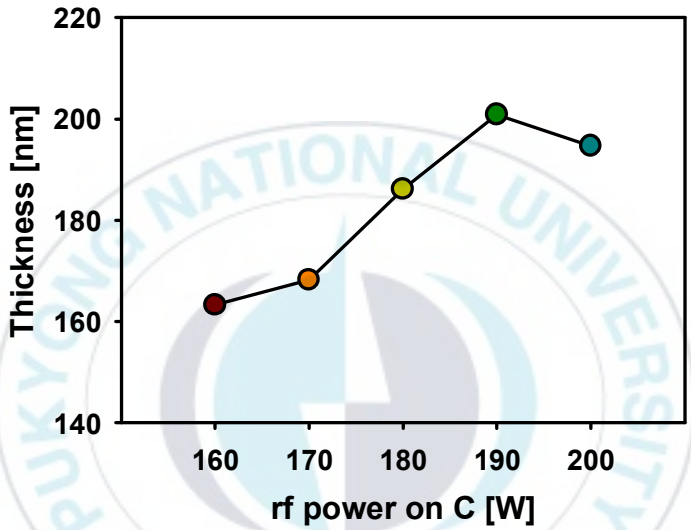

Fig. 3.1 The thickness of the MoC_x thin films as rf power on C targets changed

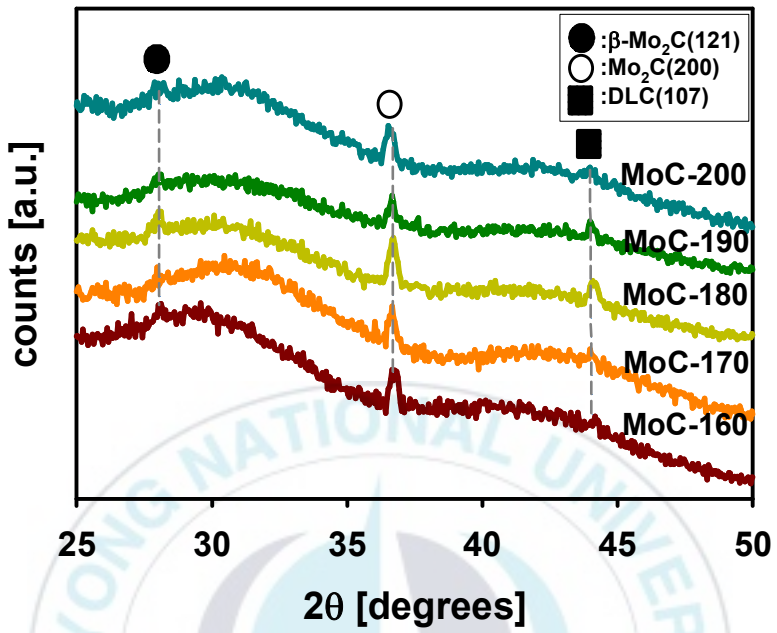

Fig. 3.2 X-ray diffraction patterns of the MoC_x thin films on the p-type Si(100) substrate

Table. 3.1 Crystallite size of the Mo_2C phase in the MoC_x thin films

Sample	Phase	FWHM [2θ degrees]	Diffraction Angle [2θ degrees]	Crystallite size [nm]
C-160	Mo_2C(200)	0.3	37.34	27.94
C-170	Mo_2C(200)	0.3	36.27	27.85
C-180	Mo_2C(200)	0.3	36.70	27.89
C-190	Mo_2C(200)	0.3	36.66	27.89
C-200	Mo_2C(200)	0.3	36.59	27.88

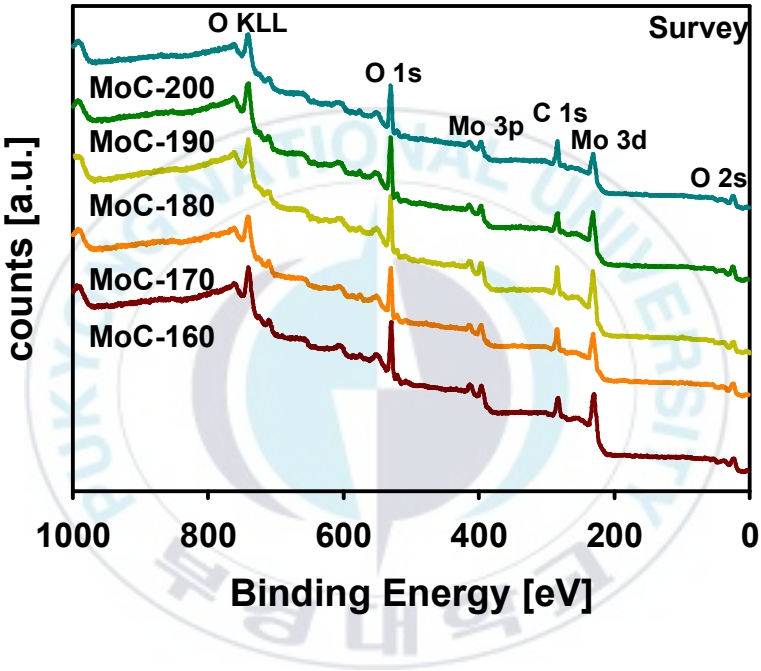

Fig. 3.3 The XPS survey spectra of the MoC_x thin films prepared with different rf power on C targets

The crystallite size was calculated by Debye-Scherrer's equation [3.24]. This peaks shifted phenomenon can be explained the structure had strain as carbon rf power increased. So, the peaks of $Mo_2C(200)$ was slightly shifted to the low diffraction angle and β-$Mo_2C(121)$ peaks decreased.

Fig. 3.3 shows the XPS survey spectra of MoC_x thin films obtained at different rf powers on C target. The characteristic XPS peaks of O, C, and Mo were observed at the binding energies of 531.0, 284.1, and 231.28 eV, respectively. So we can conclude that the sputtering process for deposition MoC_x was conducted successfully. Although pure Ar gas was used and high vacuum system was applied for co-sputtering, XPS peak of O was detected. The oxygen could be originated from the residual oxygen species in the co-sputtering chamber such as H_2O and/or CO_2. This is an indirect clue of the formation of MoC_x thin films. The XPS peak at 398.4 eV was assigned as Mo $3p_{5/2}$. In order to identify the chemical environment of MoC_x thin films, the high resolution XPS spectra of C 1s and Mo 3d were taken. Fig. 3.4(a) shows the high resolution XPS spectra of Mo 3d in MoC_x thin films. As shown in Fig. 3.4(a), Mo 3d XPS spectra of MoC_x thin films was apparently looked like triplet peaks because Mo species with different oxidation states were combined. So, for the identification of oxidation states of Mo, Mo 3d peaks were deconvoluted using XPSPEAK41. Fig. 3.4(b) shows the representative deconvoluted XPS spectra of Mo 3d. As shown in Fig. 3.4(b), the deconvoluted Mo 3d peaks were consisted of three peaks. One of the right side line, peak 1 was assigned for Mo metallic phase. The middle line with lowest intensity, peak 2 was assigned for Mo^{4+} phase. And the left side line, peak 3 was assigned for Mo^{6+} phase [3.25]. The two types of oxidation Mo were consisted with the MoC structure MoC and MoC_{1-x} and the other metallic Mo

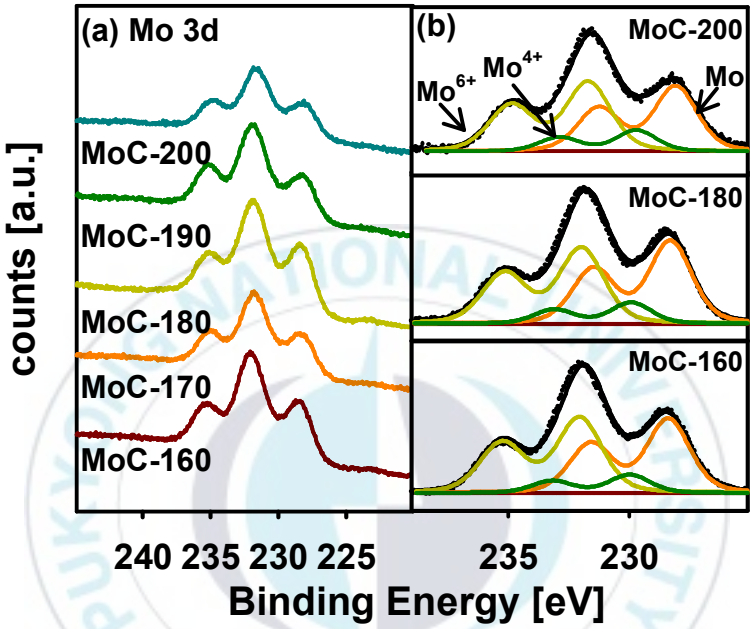

Fig. 3.4 (a) the narrow spectra of the Mo 3d in the MoC_x thin films as rf power changed, and (b) the representative deconvolution of Mo 3d peaks for finding detail oxidation information about Mo.

Table. 3.2 The portion of Mo, Mo^{4+}, and Mo^{6+} in the MoC thin films

Sample	Mo [eV]		Mo^{4+} [eV]		Mo^{6+} [eV]		Atomic ratio [%]		
	position	FWHM	position	FWHM	position	FWHM	Mo	Mo^{4+}	Mo^{6+}
MoC-160	228.38	2.10	229.98	2.00	232.05	2.20	43.46	10.23	46.31
MoC-170	228.19	2.10	229.79	2.00	231.79	2.20	42.76	10.45	46.79
MoC-180	228.21	2.10	229.85	2.00	231.92	2.20	45.31	11.11	43.58
MoC-190	228.25	2.10	229.85	2.00	231.95	2.20	40.35	7.83	51.82
MoC-200	228.00	2.10	229.64	2.00	231.64	2.20	40.48	12.81	46.71
Average	228.21	2.10	229.82	2.00	231.87	2.20	42.47	10.49	47.04

was deposited as amorphous phase. The detailed information deduced after deconvolution is listed in Table. 3.2.

Fig. 3.5(a) is the high resolution XPS spectra of C 1s of MoC_x thin films obtained at various rf powers on C target. As shown in Fig. 3.5(a), C 1s peaks were not symmetric and the shoulder peak at low binding energy of C 1s slightly increased as sputtering power of C target, so deconvolution process of C 1s peaks for detailed information was conducted. As shown in Fig. 3.5(b), representative deconvoluted spectra of C 1s was consisted of four peaks, C-Mo, C, C-O, and C=O [3.25]. C peaks, the middle line and highest intensity line were centered at 284.6 eV. Theses peaks can be used as the reference for the shifted other spectra. As shown in Table 3.3, Data of C 1s deconvolution, the portion of C-Mo was increased as the rf power increased. This phenomenon was affected by rf power likely thickness. The larger sputtering power on C target applied, the more MoC was made. The atomic ratio between C-Mo and oxidized Mo was shown in Table 3.4. The C-Mo and oxidized Mo were organized structure of Mo_2C. In order to satisfy the stoichiometry of Mo_2C, the ratio of C-Mo/oxidized Mo should be 0.5. As shown the Table 3.4, the ratio of MoC-160 was satisfied stoichiometry for the Mo_2C phase and the others ratio were over the 0.5 and going to nearly 2. This phenomenon can be explained with XRD data. $Mo_2C(200)$ phase were shifted to the lower diffraction angle because of the strain on the structure. The excess carbon was attached irregular site and gave the strain to the Mo_2C structure. Fig. 3.6 is the atomic ratio of C, O, and Mo in the MoC_x thin films. The ratio of Mo was decreased as rf power increased, from 20.0% to 13.1%. On the contrary, C ratio was increased from 43.7% to 53.8%. This phenomenon was also affected by the rf power on carbon target.

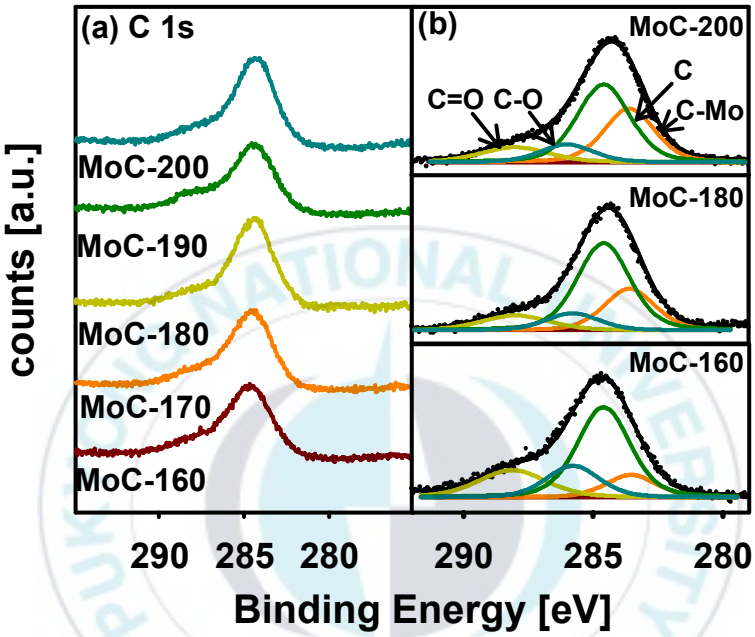

Fig. 3.5 (a) the C 1s on the MoC_x thin films, (b) is the representative deconvolution spectra of C 1s.

Table. 3.3. Detailed information about the deconvoluted peaks of C 1s on the MoC_x thin films.

Sample	C-Mo [eV]		C [eV]		C-O [eV]		C=O [eV]		Atomic ratio [%]			
	position	FWHM	position	FWHM	position	FWHM	position	FWHM	MoC	C	C-O	C=O
MoC-160	283.54	2.30	284.60	2.40	285.78	2.40	288.13	3.10	12.10	50.46	17.73	19.71
MoC-170	283.56	2.30	284.60	2.40	285.98	2.40	288.00	3.10	15.09	53.35	14.89	16.67
MoC-180	283.60	2.30	284.60	2.40	285.80	2.40	288.00	3.10	24.46	53.31	10.46	11.77
MoC-190	283.73	2.30	284.60	2.40	286.25	2.40	288.15	3.10	27.48	42.42	13.19	16.92
MoC-200	283.61	2.30	284.60	2.40	286.02	2.40	288.02	3.10	30.86	46.72	10.74	11.67
Average	283.61	2.30	284.60	2.40	285.97	2.40	288.06	3.10	22.00	49.25	13.40	15.35

Table. 3.4. The atomic percentages of Mo with different oxidation states and C-Mo in the MoC structure.

	MoC -160	MoC -170	MoC -180	MoC -190	MoC -200
Mo-C/ Oxidized Mo	0.50	0.85	1.06	1.23	2.07

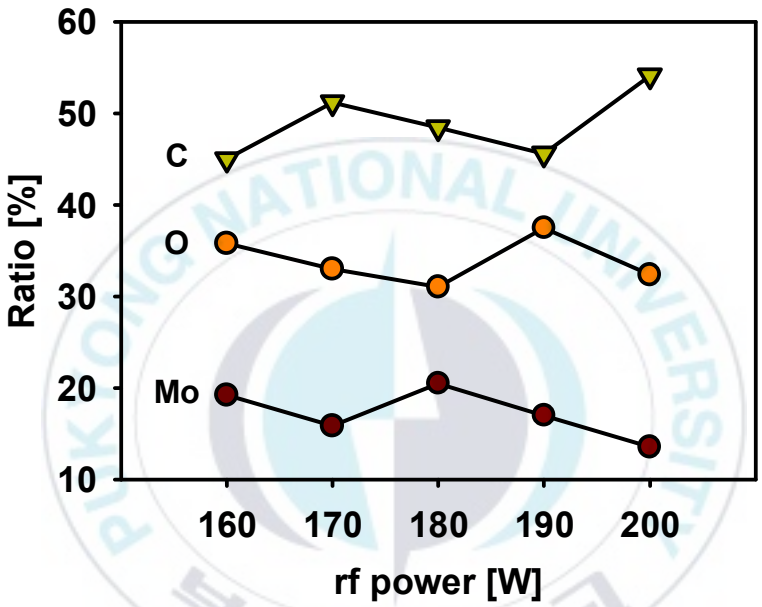

Fig. 3.6 The atomic percentages of the C, O, and Mo on the MoC_x thin films as C target power increased

Fig. 3.7 is the electrical properties of MoC_x thin films. The circle, represents conductivity of the MoC_x thin films, and the triangles was resistivity of MoC_x. The conductivity of the MoC_x thin film was affected by Mo atomic ratio. The conductivity was decreased from MoC-160 to 170, 258.68 to 128.10 S/cm as Mo ratio was decreased from 19.23 to 15.86%. And rf power was changed from 170 to 180 W as the Mo ratio was changed from 15.86 to 20.47% and conductivity was likely changed from 128.10 to 312.44 S/cm. This phenomenon can be explained the Mo is more effect to conductivity. The conductivity of the MoC_x was changed to likely Mo atomic ratio. The resistivity of MoC_x is reverse trend with conductivity.

The contact angle of the MoC_x thin films measured with DW and EG was shown in Fig. 3.8. Both of the contact angles were increased as sputtering power on carbon increased. But the more increase of the contact angle was observed with DW. Surface free energy(SFE) of MoC_x thin films was shown in Fig. 3.9 [3.26]. The circle is the total SFE, triangle is dispersive energy, and square is the polar SFE of MoC_x thin film at various rf power of C target. The polar SFE of MoC_x increase as rf power was increased. On the contrary, dispersive SFE of the MoC_x is decreased as rf power increased. Then, the total SFE was decreased as the rf power increased.

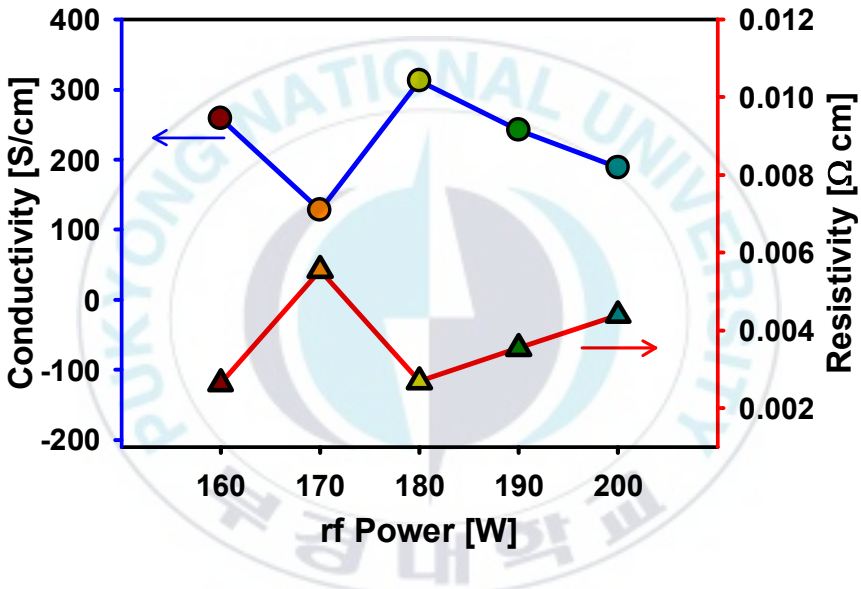

Fig. 3.7 Electrical properties of the MoC_x thin films

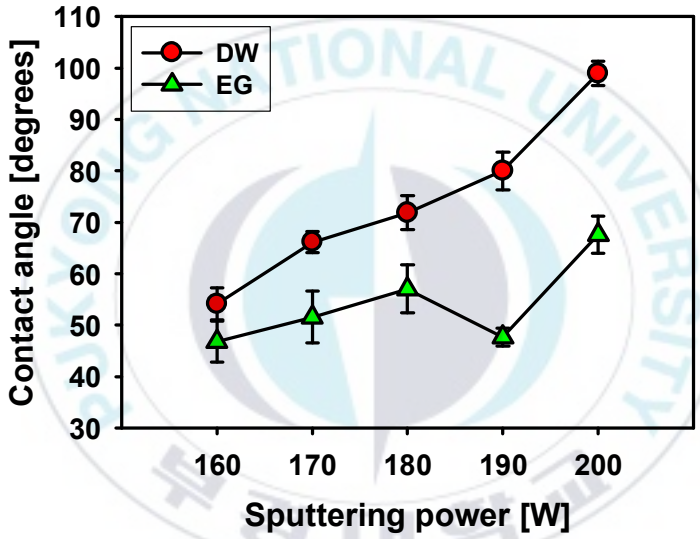

Fig. 3.8 Contact angle of the MoC_x thin films measured with distilled water and ethylene glycol.

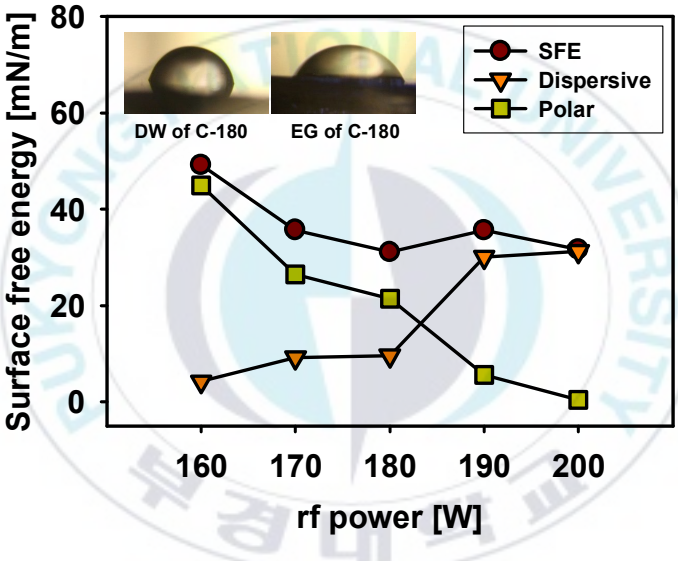

Fig. 3.9 Surface free energy of MoC_x thin films.

3.4 Conclusion

The thickness of the MoC_x thin films has increasing tendency as rf power of the C target increased measured by alpha step measurement. MoC_x has the three phase of crystallinity, DLC(107), β-Mo_2C(121), and Mo_2C(200). Mo_2C(200) phase was slightly shifted as rf power increased investigated by XRD. From XPS survey spectra, C-Mo phase in C 1s was increased as rf power increased and Mo 3d was consist of the Mo, $Mo^{4+,}$ and Mo^{6+}. Atomic ratio between C-Mo and oxidized Mo was changed from 0.5 to 2, respectively. Atomic ratio of Mo was decreased as rf power increased. On the contrary, C was increased as rf power increased. Atomic ratio of Mo affect to conductivity of MoC_x. SFE of the MoC_x thin films was decreased as rf power increased.

References

[1.1] N. C. Alov, *J. Anal. Chem.* 60 (2005) 297.

[1.2] S. G. Kumar and K. S. R. K. Rao, *Energ. Environ. Sci.* 7 (2014) 45.

[1.3] M. S. Aksenov, A. Y. Kokhanovskii, P. A. Polovodov, S. F. Decyatova, V. A. Golyashov, A. S. Kozhukhov, I. P. Prosvirin, S. E. Khandarkhaeva, A. K. Gutakovskii, N. A. Valisheva, and O. E. Tereshchenko, *Appl. Phys. Lett.* 107 (2015) 173501.

[1.4] R. Martel, T. Schmidt, H. R. Shea, T. Hertel, and Ph. Avouris, *Appl. Phys. Lett.* 73 (1998) 2447.

[1.5] M. Mizukami, S. Oku, S. Cho, M. Tatetsu, M. Abiko, M. Mamada, T. Sakanoue, Y. Suzuri, J. Kido, and S. Tokito, *IEEE. Electron Device Lett.* 36 (2015) 841.

[1.6] M. Lee, S. Hong, and D. Kim, *Appl. Surf. Sci.* 252 (2006) 5019.

[1.7] H. Koo, W. Lee, Y. Choi, J. Sun, J. Bak, J. Noh, V. Subramanian, Y. Azuma, Y. Majima, and G. Cho, *SCI. Rep.* 5 (2015) 14459.

[1.8] T. Meng, K. Young, D. Beglau, S. Yan, P. Zeng, and M. M. Cheng, *J. Power Sources* 302 (2016) 31.

[1.9] S. Choi, J. Park, E. Jeong, B. Kim, S. Son, J. Lee, J. Lee, H. Jo, J. Park, and Y. C. Kang, *J. Chosun Natural Sci.* 7 (2014) 183.

[2.1] I. Matanovic, F. H. Garzon, and N. J. Henson, *Phs. Chem. Chem. Phys.* 16 (2014) 3014.

[2.2] V. P. Anitha, A. Bhattacharya, N. G. Patil, and S. Major, *Thin Solid Films* 236

(1993) 306.

[2.3] V. P. Anitha, S. Vitta, and S. Major, *Thin Solid Films* 245 (1994) 1.

[2.4] D. K. Nandi, U. K. Sen, D. Choudhury, S. Mitra, and S. K. Sarkar, *ACS App. Mater. Inter.* 6 (2014) 6606.

[2.5] Z. Li, C. Chen, E. Zhan, N. Ta, and W. Shen, *Catal. Commun.* 51 (2014) 58.

[2.6] W. Grunert, A. Y. Stakheev, R. Feldhaus, K. Anders, E. S. Shpiro, and K. M. Minachev, *J. Phys. Chem.* 95 (1991) 1323.

[2.7] B. Zhao, K. Sun, Z. Song, and J. Yang, *Appl. Surf. Sci.* 256 (2010) 6003.

[2.8] A. Kumar, A. Singh, R. Kumar, M. Kumar, and D. Kumar, *Optoelectron. Adv. Mat.* 5 (2011) 52.

[2.9] K. Khojier, M. R. K. Mher, and H. Savaloni, *J. Nanostructure Chem.* 3 (2013) 5.

[2.10] Y. Wang, and R. Y. Lin, *Mater. Sci. Eng. B-Adv.* 112 (2004) 42.

[2.11] S. Song, Y. Liu, D. Mao, H. Ling, and M. Li, *Thin Solid Films* 476 (2005) 142.

[2.12] A. Gilewicz, B. Warcholinski, and D. Murzynski, *Surf. Coatings Technology* 236 (2013) 149.

[2.13] Y. Zhang, N. Haberkorn, F. Ronning, H. Wang, N. A. Mara, M. Zhuo, L. Chen, J. H. Lee, K. J. Blackmore, E. Bauer, A. K. Burrell, T. M. McCleskey, M. E. Hawley, R. K. Schulze, L. Civale, T. Tajima, and Q. Jia, *J. Am. Chem. Soc.* 133 (2011) 20735.

[2.14] X. Zhu, D. Yue, C. Shang, M. Fan, and B. Hou. *Surf. Coatings Technology* 228 (2013) S184.

[2.15] F. C. Carreri, R. M. Oliveira, A. C. Oliveira, M. M. N. F. Silva, M. Ueda, M. M. Silva, and L. Pichon, *Appl. Surf. Sci.* 310 (2014) 305.

[2.16] P. Hones, N. Martin, M. Regula, and F. Levy, *J. Phys. D: Appl. Phys.* 36 (2003) 1023.

[2.17] V. P. Anitha, S. Major, D. Chandrashekharam, and M. Bhatnagar, *Surf. Coatings Technology* 79 (1996) 50.

[2.18] Y. G. Shen, *Mat. Sci. Eng. A-Struct. A* 359 (2003) 158.

[2.19] J. N. Kim, S. Park, T. Kim, and J. J. Lee, *Thin Solid Film* 519 (2011) 6876

[2.20] V. V. Atuchin, T. Khasanov, V. A. Kochubey, and L. D. Pokrovsky, *Int. J. Mod. Phys. B* 23 (2009) 4817.

[2.21] D. C. Harris, *Quantitative Chemical Analysis* 8^{th} *ed.*; W. H. Freeman and Company: New York, 2010; p. 83.

[2.22] A. F. Júnior, E. C. De O. Lima, M. A. Novak, P. R. Wells Jr., N. V. Brenner, and S. V. Trubina, *Inorg. Mater.* 42 (2006) 1222.

[2.23] H. O. Pierson, *Handbook of Refractory Carbides and Nitrides*; NOYES PUBLICATIONS: New Jersey, 1996; p. 17.

[2.24] J. Park, and Y. C. Kang, *Met. Mater. Int.* 19 (2013) 55.

[2.25] L. N. Mazalov, V. V. Sokolov, Q. Mang, I. M. Oglezneva, N. V. Brenner, and S. V. Trubina, *Inorg. Mater.* 42 (2006) 1222.

[2.26] W. Grünert, A. Y. Stakheev, R. Feldhaus, K. Andrs, E. S. Shpiro, and K. M.

Minachev, *J. Phys. Chem.* 95 (1991) 1323.

[2.27] J. G. Choi, and L. T. Thompson, *Appl. Surf. Sci.* 93 (1996) 143.

[2.28] G. T. Kim, T. K. Park, H. Chung, Y. T. Kim, M. H. Kwon, and J. G. Choi, *Appl. Surf. Sci.* 152 (1999) 35.

[3.1] C. C. Tripathi, M. Kumar, and D. Kumar, *Bull. Master. Sci.* 34 (2011) 1611.

[3.2] Q. Liu, X. P. Wang, F. J. Liang, J. X. Wang, and Q. F. Fang, *Mater. Res. Bull.* 41 (2006) 1430.

[3.3] C. C. Tripathi, M. Kumar, and D. Kumar, *Appl. Surf. Sci.* 255 (2009) 3518.

[3.4] E. Bertran, C. Corbella, A. Pinyol, M. Vives, and J. L. Andujar, *Diam. Relat. Mater.* 12 (2003) 1008.

[3.5] G. D. Temmerman, M. Ley, J. Boudaden, and P. Oelhafen, *J. Nucl. Mater.* 337 (2005) 956.

[3.6] X. He, W. Li, and H. Li, *Mater. SCI. Eng. B-Adv.* 31 (1995) 269.

[3.7] Z. G. Yuan, J. F. Yang, Z. J. Cheng, X. P. Wang, and Q. F. Fang, *Surf. Coat. Tech.* 231 (2013) 14.

[3.8] A. Villa, S. Campisi, C. Giordano, K. Ote, and L. Prati, *ACS Catal.* 2 (2012) 1377.

[3.9] A. Hanif, T. Xia, A. P. E. York, J. Sloan, and M. L. H. Green, *Chem. Mater.* 14 (2002) 1009.

[3.10] L. Ji, H. Li, F. Zhao, W. Quan, J. Chen, and H. Zhou, *Appl. Surf. Sci.* 255 (2009)

4180.

[3.11] H. Y. Chen, L. Chen, Y. Lu, Q. Hong, H. C. Chua, S. B. Tang, and J. Lin, *Catal. Today.* 96 (2004) 161.

[3.12] K. Karlsruhe, *J. Low. Temp. Phys.* 69 (1987) 257.

[3.13] C. Corbella, M. Vives, A. Pinyol, E. Bertran, C. Canal, M. C. Polo, and J. L. Andujar, *Surf. Coat. Tech.* 177 (2004) 409.

[3.14] K. Baba, and R. Hatada, *Surf. Coat. Tech.* 196 (2005) 207.

[3.15] C. A. Wolden, A. Pickerell, T. Gawai, S. Parks, J. Hensley, and J. D. Way, *ACS Appl. Mater. Interfaces* 3 (2011) 517.

[3.16] E. Lucazeau, A. Deneuville, J. Fontenile, F. Brunet, and E. Gheeraert, *Diam. Relat. Mater.* 5 (1996) 779.

[3.17] C. Corbella, G. Oncins, M. A. Gomez, M. C. Polo, E. Pascual, J. Gracia-Cespeds, J. L. Andujar, and E. Bertran, *Diam. Relat. Mater.* 14 (2005) 1103.

[3.18] C. Blomfield, B. Tielsch, and L. Y. C. Tan, *J. Appl. Phys.* 86 (1999) 4871.

[3.19] E. L. Hasse, *J. Low. Temp. Phys.* 69 (1987) 245.

[3.20] N. S. Alhjri, D. H. Anjum, and K. Takanabe, *J. Mater. Chem.* A 2 (2014) 10548.

[3.21] L. Ji, H. Li, F. Zhao, J. Chen, and H. Zhou, *Diam. Relat. Mater.* 17 (2008) 1949.

[3.22] D. C. Harris, *Quantitative Chemical Analysis 8th ed.*; W. H. Freeman and Company: New York, 2010; p. 83.

[3.23] H. O. Pierson, *Handbook of Refractory Carbides and Nitrides*; NOYES PUBLICATIONS: New Jersey, 1996; p. 34.

[3.24] A. F. Júnior, E. C. De O. Lima, M. A. Novak, P. R. Wells Jr., N. V. Brenner, and S. V. Trubina, *Inorg. Mater.* 42 (2006) 1222.

[3.25] C. Anandan, L. Mohan, and P. D. Babu, *Appl. Surf. Sci.* 296 (2014) 86.

[3.26] C. W. Fan, and S. C. Lee, *J. Adhes. Sci. Technol.* 24 (2010) 255.

몰리브데넘의 질화물 및 탄화물 박막

정은강

부경대학교 대학원 화학과

요약

몰리브데넘의 질화물 (MoN_x) 박막은 초고진공 상태의 챔버에서 다양한 질소 압력상태 하에서 반응성 고주파 마그네트론 스퍼터링 방법을 통해 p-type Si(100) 기판 위에 증착 하였다. 스퍼터링 기체 내에 질소의 첨가가 없을 경우, Mo(110)과 Mo(211)인 금속상이 확인되었다. 단차두께측정기로 측정한 박막의 두께는 스퍼터링 기체 내의 질소의 비율이 0에서 100%로 증가함에 따라 186.0 에서 21.5 nm로 감소하는 것을 알 수 있었다. X-선 광전자분광기 분석을 통해 몰리브데넘의 산화상태가 질소의 비율이 증가함에 따라 더욱 산화된다는 것을 알 수 있었다. 질소 비율이 증가함에 따라 Mo^{4+}가 감소하는 반면에, Mo^{5+}와 Mo^{6+}가 증가하였다. 질소의 비율이 증가함에 따라 MoN_x 박막이 생성되는 것을 질소 1s의 XPS 분석을 통해 알 수 있었다. 또한 전도도는 질소의 비율에 따라 927.7 에서 97.1 S/cm로 감소하였다.

몰리브데넘의 탄화물 (MoC_x) 박막은 고주파 마그네트론 코-스퍼터링 방법으로 고진공 챔버에서 증착되었다. 다양한 rf power의 변화에 따라 증착 된 MoC_x 박막을 비교해 봤다. MoC_x 박막의 두께는 163.3 에서 194.86 nm로 스퍼터링 파워의 160에서 200 W의 변화와 동일하게 증가하였다. X-선 회절분석기를 통해 MoC_x 박막이 β-Mo_2C, Mo_2C, 그리고 diamond like carbon (DLC) 상을 가지고 있는 것을 확인하였다. 또한 몰리브데넘 3d와 탄소 1s의 고분해능 분석을 통해 MoC_x 박막이 잘 만들어 졌다는 것을 확인 하였다. 몰리브데넘 3d 피크는 금속성 Mo, Mo^{4+}, 그리고 Mo^{6+}로 구성되어있다. 그리고 탄소 1s 피크는, C-Mo, C, C-O, 그리고 C=O의 상태로 확인되었다.

Acknowledgement

가장 먼저 대학원 기간 내내 저를 가르쳐주시고 돌보아 주셨던 강용철 교수님께 감사 드립니다. 백지에 가까웠던 저에게 A 부터 Z까지 하나하나 세세하게 가르쳐 주시고 또한 삶에 있어서도 차분함, 겸손, 그리고 부지런함을 항상 알려주신 교수님 덕분에 힘들고 많은 일들이 있었던 지난 2년간을 올바르게 마무리 할 수 있었음에 감사 드립니다. 또한 김주창, 변상용 교수님에게도 감사 드립니다. 학부시절 공부에 대한 열정을 알려주신 변상용 교수님과 수업시간과 삶에 있어서 바라만 봐도 좋은 영향력을 받을 수 있었던 김주창 교수님께 또한 감사 드립니다.

그리고 SMIL 식구 들에게 감사 드립니다. 입학부터 졸업까지 항상 많은 지도와 부지런함을 몸소 보여주었던 박주연박사님께 감사 드리고, 먼저 졸업한 서보열 형님, 최수진에게도 감사 드립니다. 두 사람이 보여주었던 석사생활의 모습들이 있었기에 저 또한 그 모습을 따라서 잘 성장한 것 같습니다. 감사합니다. 그리고 후배로 들어온 강유진과 최아롬 에게도 감사합니다. 항상 말했듯이 둘은 서로 보완하며 잘 해낼 것을 믿어 의심치 않습니다.

2년동안 함께했던 대학원생들에게도 감사합니다. 특히 황태경, 구본원, 김동우, 김종민, 오성훈 등 남자 대학원생들에게 감사합니다. 나이의 많고 적음을 떠나서 항상 자신의 것들에도 바쁘지만 많은 도움들과 교류를 해주었기에 대학원대표 역할을 할 때나 그 후에나 저의 일에 있어서 막힘이 없었다고 생각합니다. 너무나 감사합니다.

대학원 생활을 같이했고 지금도 하고 있는 동기들, 최문석, 이슬기, 윤성근, 장인승, 지성경, 장재현, 그리고 양재영에게 감사합니다. 힘들고 그리고 삶에 있어서 힘주고 즐기는 동안에 2년이 무사히 지나갔습니다, 감사합니다.

그리고 항상 즐겁게 활동했던 화학과 축구팀 C1, 농구팀 C1, 그리고 가끔씩 함께했던 야구팀 초토화 학생들 모두에게 감사합니다. 앞으로도 운동과 함께 자기 꿈들을 이루어 나갔으면 좋겠습니다.

가족들에게도 감사합니다. 천둥벌거숭이 같은 저의 고집에 또 한번 고생하셨고, 항상 마음 졸이시면서 뒤에서 기도 해주신 것에 너무나 감사합니다. 아버지, 어머니, 누나, 그리고 늦은 시간 돌아오면 반겨주던 토미까지 모든 가족이 행복하게 보낼 수 있도록 더욱 노력하겠습니다.

그리고 김수지에게 감사합니다. 본인의 중요한 시기에도 저를 챙겨주면서 함께 많은 시간을 이겨낸 것 같습니다. 김수지를 통해서 많은 것이 변했고, 특히 차분함을 통해서 삶의 방향성이 올바르게 나아가고 있음을 느낍니다. 둘이서 끊임없이 노력한 끝에 석사라는 학위와 약대라는 꿈을 모두 이룰 수 있었습니다. 항상 감사하고 또 감사합니다.

이외에도 석사 기간과 저의 삶에 영향을 미친 모든 분들에게 감사합니다.